RSC Advances

ROYAL SOCIETY OF CHEMISTRY

www.rsc.org/advances

Journal Name

RSCPublishing

ARTICLE

Composite Titanate Cathode Decorated with Heterogeneous Electrocatalytic Sites Towards Efficient Carbon Dioxide Electrolysis

Jun Zhang,[a] Kui Xie,[a, b] * Yong Zhang, [a, b] Liming Yang, [a] Guojian Wu, [a] Qingqing Qin, [a, b] Yuanxin Li, [a] Yucheng Wu [a, b] *

Cite this: DOI: 10.1039/x0xx00000x

Received 00th January 2012,
Accepted 00th January 2012

DOI: 10.1039/x0xx00000x

www.rsc.org/

The coupling of surface oxygen vacancy with nano-sized metal can effectively improve catalytic activity of heterogeneous catalyst. In this work, the high concentration of oxygen vacancy is created in Mn-doped titanate cathode, then iron nanoparticles are exsolved to anchor on the titanate surface and combine the surface oxygen vacancies to form heterogeneous catalysis clusters. The active Mn in the B site of the redox-stable $Sr_{0.95}Ti_{0.8}Nb_{0.1}Mn_{0.1}O_{3.00}$ (STNMO) creates 0.15 mol oxygen vacancies in the reduced $Sr_{0.95}Ti_{0.8}Nb_{0.1}Mn_{0.1}O_{2.85}$. With iron doping in the B site, it is found that the exsolution and dissolution of the iron nanoparticles is completely reversible on titanate surface in redox cycles. The presence of iron nano crystal remarkably increases the ionic conductivity of the titanate solid solution by 0.5 order of magnitude at intermediate temperatures. Promising electrode polarizations are obtained based on the titanate cathode decorate with heterogeneous electrocatalytic clusters in symmetric cells. The current efficiencies of direct carbon dioxide electrolysis reaches as high as 90% in an oxide-ion conducting solid oxide electrolyzer at high temperatures.

Introduction

Solid oxide electrolyzers have shown huge advantages of electrochemical conversion of carbon dioxide with high efficiency using renewable electrical energy.[1-4] Under external potential, CO_2 molecules are electrochemically reduced into CO in cathode while the O^{2-} ions are transported through the oxygen-ion conducting electrolyte to anode where the O_2 gas is formed and released.[5,6]

Traditional Ni/YSZ composite cathode has demonstrated excellent performances for high temperature electrolysis of CO_2 in solid oxide electrolyzers.[7,8] Nevertheless, the Ni/YSZ cermets require a significant concentration of reducing gas flowing over the cathode to avoid the oxidation of Ni to NiO. In contrast to Ni/YSZ, the perovskite-type $La_xSr_{1-x}Cr_yMn_{1-y}O_{3-\delta}$ (LSCM) is an active and redox stable material which has been utilized for the direct high-temperature electrolysis and promising electrode polarizations have been achieved.[9,10] We have recently demonstrated the direct high-temperature electrolysis of CO_2 using LSCM cathode without the flow of reducing gas over the electrode in an oxide-ion conducting

solid oxide electrolyzers and found that the strong reducing potentials required for CO_2 splitting cause the chemical and structural changes of the p-type LSCM and therefore exhibit large electrode polarization resistance and decreased *Faradic* current efficiencies at high applied potentials.[11,12]

On the other hand, the perovskite titanate, e.g., $La_xSr_{1-x}TiO_{3+\delta}$ (LSTO), has been considered as the breakthrough in the field of solid oxide fuel cells.[13] The LSTO has pretty high n-type conductivity upon reduction and has been proved to be an alternative electrode material for solid oxide electrolyser.[13] Composite cathode based on $La_{0.2}Sr_{0.8}TiO_{3.1}$ has been confirmed to be well adapted to the reducing condition for the efficient electrolysis of CO_2 in an oxygen-ion conducting solid oxide electrolyser because the $La_xSr_{1-x}TiO_{3+\delta}$ is partially electrochemically reduced ($Ti^{4+} \rightarrow Ti^{3+}$) at potentials required for CO_2 reduction and the n-type electronic conduction of composite cathode is accordingly enhanced.[14] Nevertheless, the insufficient catalytic activity still limits the electrode polarization and current efficiency for the high temperature electrolysis.[14] Similarly, the niobium doped titanate, i. e. $SrTi_{0.9}Nb_{0.1}O_3$ has also shown pretty high electronic conductivity (340 $S \cdot cm^{-1}$ in reducing situation at high temperature) and promising electrochemical properties.[15,16] The doping of Nb in the B site is expected to significantly improve the electrical properties. Gross et al reported the excellent redox stability of $SrTi_{0.99}Nb_{0.01}O_3$ even after reduction in humidified H_2 (3% H_2O) atmosphere and then oxidization at 800 ^oC in air.[16] Composite electrode based on titanate is therefore utilized as cathode for high temperature electrolyser or the anode of solid oxide fuel cells (SOFCs).[17,18] Mogensen et al. reported that the Nb-doped strontium titanates as a part of a SOFC anode showed promising redox stability features.[18]

In a solid oxide carbon dioxide electrolyzer, the insufficient adsorption of CO_2 is always the limitation at high temperature that leads to the local starvation of CO_2 and therefore restricts the cell performance and current efficiency because the linear CO_2 molecules without any polarity are hard to be chemically adsorbed and activated especially at high temperatures.[19] It is common to observe that the local starvation of CO_2 mainly leads to the large electrode polarizations and low current efficiencies for the electrolysis of CO_2 at high temperature. It is reported that the mass transfer is always the limiting step of the electrolysis of CO_2 at higher applied potentials according to their *in-situ* AC impedance studies and the nano-structured composite cathode with extended three-phase boundaries can relieve the local starvation of CO_2 to some extent.[20,21] We have recently reported that the remarkable chemical adsorption of CO_2 can be achieved on Mn-doped titanate and the onset temperature of strong chemical desorption is then extended to as high as approximately 800 °C of the common operation temperature of solid oxide carbon dioxide electrolyzers.[22] The active Mn with oxidation states in the B-site lattice creates sufficient oxygen vacancies to accommodate and activate the CO_2 molecules. The ionic conductivities of the Mn-doped titanate are remarkably enhanced by 1 order of magnitude at high temperatures.[22] The current efficiencies are then significantly improved with the Mn-doped titanate cathode for the direct electrolysis of CO_2 in an oxide-ion conducting solid oxide electrolyser.

Conventional Ni or Fe nanocrystals are commonly utilized as the excellent catalysts for electrocatalyst at higher temperatures in the field of electrolysis of H_2O or CO_2.[23-25] These nano sized metals are also widely loaded on some oxygen-deficient ceramic substrates including $CeO_{2-\delta}$ and $Ce_xZr_{1-x}O_{2-\delta}$ powders to form heterogeneous catalysis clusters.[26] The coupling of metallic nanoparticles and ceramic substrates significantly enhance the heterogeneous catalytic activity because of the combination of the excellent catalytic activity

of the nano-sized metal and the efficient accommodation/activation of reactant molecules in the oxygen-deficient sites on the substrate surfaces.[27] The loading of nano metals on ceramic material surface is also expected to largely enhance the conductivity at intermediate temperatures as worked by Liu et al.[28] The method to incorporate the catalyst as a dopant within a host lattice during the synthesis in air, which is then exsolved at the surface in the form of catalytically active metallic nanoparticles or micron-particles under reducing conditions, has been recently reported to prepare metal nanocrystal loaded composite electrode for solid oxide fuel cell anode and solid oxide electrolyzer cathode.[29-31] Upon re-oxidation, the dopant is re-incorporated into the host lattice, yielding a regenerative catalyst in the composite electrode. The coupling of exsolved metallic nanoparticles and the surface oxygen vacancy is therefore expected to significantly enhance the electrochemical performances of the composite electrode.

In this work, the Mn and Fe are co-doped in the titanate $Sr_{0.95}Ti_{0.9}Nb_{0.1}O_3$ in which the Mn is utilized to create sufficient oxygen vacancies while the Fe nanocrystal is then exsolved to anchor on the titanate surface after reduction. The crystal structures and electrical properties of the samples are systematically investigated. The reversible exsolution of iron nanocrystal is then studied. Direct electrolysis of CO_2 with the composite cathode is then performed in an oxide-ion conducting solid oxide electrolyzer at high temperature.

Experimental

In this experiment, all the chemicals (99.9%, AR) were purchased from SINOPHARM Chemical Reagent Co. Ltd (China). The $(Sr_{0.95})_{0.9}(Ti_{0.8}Nb_{0.1}Mn_{0.1})_{0.9}Fe_{0.1}O_{3-\delta}$ (STNMFO) powders were synthesized by a high-temperature solid state reaction method.[32] Proper stoichiometric amounts of $SrCO_3$, TiO_2, Nb_2O_5, MnO_2 and Fe_2O_3 powders were mixed together and ball milled for 30 min in acetone, then the dried powders were pressed into pellets under ~4MPa and fired at 1300 ^oC for 10 h in air. The powders of $Sr_{0.95}Ti_{0.8}Nb_{0.1}Mn_{0.1}O_3$ (STNMO) were synthesized as the same way as described above. The $(La_{0.8}Sr_{0.2})_{0.95}MnO_{3-\delta}$ (LSMO) were prepared using the same method as described above by mixing the stoichiometric amounts of La_2O_3, $SrCO_3$ and $MnO_2$and the treatment temperature was 1100 ^oC for 10 h in air.[33] The $Ce_{0.8}Sm_{0.2}O_{2-\delta}$ (SDC) powders were prepared by the combustion method in which the Sm_2O_3 and $Ce(NO_3)_3{\cdot}6H_2O$ powders were mixed evenly and sintered at 800 ^oC for 3 h in air.[34] All the phase formation of STNMFO, STNMO, LSMO and SDC powders were analyzed by X-ray diffraction (XRD, $2\theta=3^o{\cdot}min^{-1}$, D/MAX2500V, Rigaku Corporation, Japan). High-resolution Transmission Electron Microscopy (HRTEM) analysis with selected area diffraction was performed to observe the oxidized and reduced STNMFO and STNMO powders with a JEOL 2100F field emission transmission electron microscope operated at 200 kV. In addition, X-Ray Photoelectron Spectroscopy (XPS) was performed on a Thermo ESCALAB 250 to analyze the surface of the oxidized and reduced STNMFO and STNMO sample powders, the binding energies were calibrated to the C1s peak at 284.6 eV.

Approximately 2.5 g STNMFO and STNMO powders were pressed into disks under 6-8 MPa and then sintered at 1300 ^oC for 10 h in air for the ionic conductivity test. The relative density of the sintered samples reached approximately 85-90%. The ionic conductivity of samples was tested *versus* temperature using the electron-blocking electrode method, respectively.[35,36] Before the ionic conductivity test, the disks of STNMFO and STNMO were reduced at 1400 ^oC for 10 h in 5%H_2/Ar, respectively. The DC four-terminal method was used for conductivity test for the reduced samples in the reducing atmosphere (5%H_2/Ar) and oxidized

samples in the oxidizing atmosphere (air). The temperature was ranging from 400 to 800 ^{o}C with a step of 3 ^{o}C·min^{-1} while the conductivity was recorded with an online multi-meter (Keithley 2000, Digital Multimeter, Keithley Instruments Inc., USA) at a time step of 10 s. The conductivity was recorded *versus* temperature from 400 to 800 ^{o}C.

The YSZ electrolyte support with thickness of 1 mm was made by dry-pressing the YSZ powders into a green disk with a diameter of approximately 15 mm, followed with a sintering at 1550 ºC (2 ºC·min^{-1}) for 20 h in air. The two surfaces of the electrolyte were mechanically polished and ultrasonically washed in the ethanol and distilled water. The slurries of cathode STNMFO/SDC or STNMO/SDC were prepared by milling STNMFO or STNMO powders with SDC powders at a weight ratio of 65:35 in alpha-terpineol with the appropriate amount of cellulose additive.[37,38] The LSMO and SDC powders were also mixed together at a weight ratio of 65:35 in alpha-terpineol with the appropriate amount of cellulose additive to prepare the anode slurry. Then, the two kinds of slurries were coated onto the two sides of the electrolyte in the area of approximately 1 cm^2 and the sample was sintered at 1000 ^{o}C for 3 h in air. The current collector of silver paste (SS-8060, Xinluyi, Shanghai, China) was printed on both surfaces of the electrodes. The silver wire (0.4 mm in diameter) was used to form the circuit by conductive adhesive (DAD87, Shanghai Research Institute for Synthetic Resins, Shanghai, China), and treated at 550 ^{o}C for 0.5 h in air. The symmetric cell was prepared in the above same way. The AC impedance spectroscopy for the different symmetric cells were studied at the open circuit voltage (OCV) in different H_2 and CO partial pressure at 800 ^{o}C using the Electrochemical Station (IM6, Zahner, Germany). The flow rates of the gases at 20 ml·min^{-1}and different hydrogen and CO partial pressure were controlled by the mass flowmeter (D08-3F, Sevenstar, Beijing, China). The electrolysis cells were sealed to a homemade testing jig using ceramic paste (JD-767, Jiudian, Dongguan, China) for electrochemical test. The CO_2 electrolysis in the solid oxide electrolyzer based on the STNMFO/SDC and STNMO/SDC cathode was tested under different applied voltages (from 1.2 to 2.0) at 800^{o}C in CO_2. The *in-situ* AC impedance spectroscopy and the current density *versus* voltage curve (I-V curve) of the electrolysis cell were recorded. The online gas chromatograph (GC9790II, Fuli, Zhejiang, China) was used to analyze the CO concentration of the output gas from the electrolyzer cells.

Results and discussion

Fig. 1 (a1) and (a2) show the XRD Rietveld refinement patterns of the oxidized and reduced STNMO powders, respectively. The refinement of the oxidized and reduced samples give the χ^2, wRp and Rp values of 1.452, 6.09% and 4.71% and 1.748, 6.74% and 4.87%, respectively, indicating a close fit to the experimental data. Based on experimental and calculated results, it indicates that phase structure of both oxidized and reduced samples can be determined as perovskite structure with space group of Pm-3m, consistent with the standard data of XRD data (PDF: 35-0734). The crystal cell parameter of the oxidized STNMO is 3.91515(5) Å which is slightly smaller than that of the reduced STNMO, 3.91913(29) Å. In the oxidized STNMO, the chemical oxidation states of the Ti and Mn are +4 with ionic radii of 0.605 Å and 0.53 Å, the oxidation state of Nb is +5 with 0.64 Å. In contrast, a part of the Ti, Nb and Mn have been transformed to Ti^{3+} (0.67Å), Nb^{4+} (0.68 Å) and Mn^{3+} (0.645 Å) in the reduced STNMO sample which may cause the lattice expansion though the oxygen loss is present after the high-

temperature reduction. Nevertheless, no phase transition is observed in the STNMO even after the high-temperature treatment in reducing atmosphere, firmly verifying superior redox stability of STNMO ceramics. As shown in Fig. 1 (b1) and (b2), XRD Rietveld refinement patterns of single-phase STNMFO reveal the successful partial replacement of Ti by Fe in the B-site. The refinement of the oxidized and reduced samples give χ^2, wRp and Rp values of 1.220, 6.88% and 5.19% as well as 1.013, 4.98% and 3.90%, respectively. The cell parameter is 3.91574(9) Å for the oxidized STNMFO which is larger than that of the oxidized STNMO sample. This is because of the larger ionic radii of the Fe^{3+} (0.645Å) in contrast to the Ti^{4+}, Nb^{5+} and Mn^{4+} with the same coordination numbers. After reduction, most Fe^{3+} ions are reduced into Fe^0 (PDF: 65-4899, α-Fe) as shown in Fig. 1 (b2), the peak at 44.7^o corresponds to iron metal indicating successful exsolution of iron nanoparticles from STNMO substrate, which suggests excellent stability of the parent material even though the doped metal is exsolved from lattice to anchor on the reduced STNMO surface. In addition, the cell parameter of the reduced STNMFO is increased to 3.92409(4) Å not only because of the partial transformation of the Nb^{5+}, Mn^{4+} and Ti^{4+} into Nb^{4+} (0.74 Å), Mn^{3+} (0.645 Å) and Ti^{3+} (0.67Å) leading to the lattice expansion of the reduced samples but also because of the tiny residual of Fe^{2+} (0.78 Å) in lattice even after the reduction treatments.

As shown in Fig.2 (a1) and (a2), high resolution transmission electron microscopy (HRTEM) analysis of the oxidized and reduced STNMO has revealed lattice spacing of 0.276 nm (110) and 0.279 nm (110), respectively, consistent with the separation spacing determined by the XRD analysis in Fig. 1 (a1) and (a2). The corresponding lattice spacing of the oxidized has increased from 0.278 nm (110) to the 0.283 nm (110) for the reduced STNMFO in Fig. 2 (b1) and (b2), further confirming the lattice expansion of the reduced sample as determined by the XRD analysis in Fig.1 (b1) and (b2). Moreover, it can be clearly seen that the reduction of the STNMFO leads to the *in-situ* growth of iron nanoparticle on the STNMO surface in Fig.2 (b2). The analysis result of the iron has revealed lattices pacing of 0.202 nm (110), consistent with the standard data of XRD data (PDF: 65-4899). These TEM results further demonstrate and validate the reversible exsolution of iron particles on the ceramic substrate as confirmed by the XRD. More importantly, the TEM result reveals that the iron particles are exsolved to *in-situ* grow and anchor on the surface of electronically conducting STNMO, which is able to avoid any possible agglomeration of exsolved iron nanoparticles on the substrate surface at high temperatures. The iron nanoparticles can be re-incorporated or re-exsolved into/from the host material, yielding a regenerative catalyst by periodically exposing the material to oxidizing/reducing conditions.

In order to investigate the chemical state of the elements in samples after redox cycles, XPS is performed to test the oxidized and reduced STNMO and STNMFO as shown in Fig. 3 and 4, respectively. All XPS results are fitted using a Shirley-type background subtraction method, and the background functions for different XPS spectra are fitted by 80% Gaussian and 20% Lorenz. All information of XPS peak comes from the database of *Thermo Fisher Scientific*. In Fig. 3, the strong peaks of Ti^{4+}, Nb^{5+} and Mn^{4+} are observed in the oxidized STNMO, respectively. In contrast, part of Ti^{4+} is chemically reduced into Ti^{3+} while most of the Nb^{5+} and Mn^{4+} are reduced into Nb^{4+} and Mn^{3+} by treating the STNMO samples in reducing atmosphere as confirmed by the signal of Ti^{3+}, Nb^{4+} and Mn^{3+}, which is expected to significantly contributes to electrical conductivity. Similar chemical state change of Ti, Nb and Mn elements have also been observed in STNMFO sample before and after reduction at high temperature as shown in Fig. 4. In addition, the XPS spectrum of iron element is presented in Fig. 4

(d1) and (d2). The iron in the oxidation state of the STNMFO is in the form of Fe^{3+} as showed in Fig. 4 (d1); however, the Fe^0 (2p1/2) and Fe^0 (2p3/2) peaks are observed at 720.2 and 707.5 eV as shown in Fig. 4 (d2), respectively. The results of XPS show that the iron element mainly exists in the form of metal in the reduced sample, which firmly confirms the successful exsolution of iron nanocatalyst as also confirmed by the XRD and TEM results. In addition, the signal of Fe^{3+} and Fe^{2+} are also observed in Fig. 4 (d2), which indicates that small part of Fe^{3+} is only chemically reduced into Fe^{2+} by treating the STNMFO samples in reducing atmosphere.

In Fig. 5, the oxidized $Sr_{0.95}Ti_{0.9}Nb_{0.1}O_3$ (STNO) demonstrated a 0.73% weight loss when heated in reducing gas (5%H_2/Ar) from 1000 ^oC to room temperature (RT), indicating a chemical formula of $Sr_{0.95}Ti_{0.9}Nb_{0.1}O_{2.90}$ for the reduced sample. By contrast, the reduced STNMO demonstrates a chemical formula of $Sr_{0.95}Ti_{0.8}Nb_{0.1}Mn_{0.1}O_{2.85}$, which suggests that the Mn^{4+} in the oxidized sample has been completely reduced into Mn^{3+} accompanied by the generation of oxygen vacancies and the change of the coordination number of the Mn ion in the B site.

As shown in Fig. 6 (a1) and (a2), XRD results show that the crystal structure of STNMO is pretty stable even repeatedly oxidized in air at 1300 ^oC for 10 hours and then reduced in 5%H_2/Ar at 1400 ^oC for 10 hours for 2 cycles. This clearly confirms the superior redox stability of the samples even after doping of 10% Mn in the B site of the perovskite. In addition, SEM results indicate that the STNMO sample is extremely dense and uniform without any microstructure deconstruction after the 2 redox cycles as in Fig. 6 (b1) and (b2). By contrast, a reversible exsolution of iron is confirmed by XRD when the oxidized sample is repeatedly reduced as shown in Fig. 7 (a1 and a2). Moreover, SEM observation of the reduced STNMFO sample further confirms the exsolution of iron nanoparticles anchoring on the surface of the reduced STNMO as shown in Fig. 7 (b1) and (b2). The EDS mapping again validates the presence of anchored iron nanoparticles while other elements are homogeneously dispersed in the sample which suggests that no phase segregation or element agglomeration exists in the sample after the exsolution of iron nanoparticles. The coupling of iron nano crystal with the surface oxygen vacancy in reduced STNMO is expected to form heterogeneous electrocatalytic sites and therefore improve the electrode activity.

Fig.8 (a) shows the temperature dependence of ionic conductivity of the oxidized and reduced STNMO in air and 5%H_2/Ar from 400 to 800 ^oC, respectively. The ionic conductivities of the oxidized and reduced STNMO improve with temperature and finally reach 4.27×10^{-4} and 3.98×10^{-3} $S\cdot cm^{-1}$ in air and 5%H_2/Ar at 800^oC, respectively. The reduced sample has higher concentration of oxygen vacancy because of the reduction of Mn^{4+} to Mn^{3+} as confirmed by the XPS, which therefore leads to the higher ionic conductivity of the reduced STNMO. In Fig. 8 (b), the ionic conductivities of the oxidized and reduced STNMFO reach 4.83×10^{-4} and 7.03×10^{-3} $S\cdot cm^{-1}$ in air and 5%H_2/Ar at 800 ^oC, respectively. The ionic conductivity of oxidized STNMFO is higher than the oxidized STNMO due to the iron doping that creates oxygen vacancy and therefore causes positive effect on the ionic transport. In other words, the replacement of Ti^{4+} with Fe^{3+} in B site of the titanate creates oxygen vacancy as the charge carrier for the oxide ion transport in sample. However, the reduced STNMFO sample shows remarkably high ionic conductivity of 7.03×10^{-3} $S\cdot cm^{-1}$ which is 1 order of magnitude higher than the oxidized STNMFO in air and 1 time higher than the reduced STNMO in a reducing atmosphere at intermediate temperatures. Upon reduction, the STNMFO changes into a composite composed of nano-sized iron metal anchored reduced STNMO. The ionic conductivity is largely enhanced in the presence of the exsolved iron nanoparticles on the Mn-doped titanate

surface which is because the catalytic-active iron nanocrystal facilitates the ionic transport. Fig. 9 (a1) and (a2) present the microstructure of the YSZ electrolyte-supported symmetrical cells with the STNMO and STNMFO electrodes. The configurations of solid oxide electrolyzers with STNMO/SDC and STNMFO/SDC cathode are shown in Fig. 9 (b1) and (b2), respectively. The porous electrode layers are approximately 10 μm in thickness and the YSZ electrolyte supports are quite uniform and dense with the porous electrode layers adhered to the electrolyte very well.

Fig. 10 shows the AC impedance of the symmetric cells based on the STNMFO and STNMO cathodes tested at 800 ^{o}C at different hydrogen partial pressure (pH_2=10%, 20%, 40%, 60%, 80% and 100%). There are two intercepts with real axis in the impedance spectra in which the series resistant of the cell (R_s) corresponds to the first intercept and the difference between the two intercepts is a measure of the electrode polarization resistance (R_p). Generally, two semicircles will be found from R_p: the high-frequency arcs (R_1) and low-frequency arcs (R_2). The R_1 is an indication of charge transfer at high frequency and it is observed that the mass transfer dominates the electrode process of the solid oxide electrolyzers at low frequency. The R_2 is resulted from the dissociative adsorption, gas conversion, gas diffusion and species transfer at three-phase boundary. The R_s which mainly comes from the ionic resistance of the YSZ electrolyte is generally stable in a wide range of pH_2. Nevertheless, as shown in Fig. 10 (a1) and (a2), the R_p of the symmetric cell based on STNMO decreases from approximately 12.15 to 2.4 Ω·cm^2 with the pH_2 ranging from 10% to 100%, indicating that the stronger reducing atmosphere is beneficial to the improvement of the electrode polarizations. The stronger reducing atmosphere is favourable to the reduced STNMO leading to improved electrode performances. In contrast, the R_p of the symmetric cell based on STNMFO significantly improves from about 4.88 to 0.81 Ω·cm^2 with increasing pH_2, which is probably due to the enhanced electrocatalytic activity of this composite electrode in the presence of nano-sized iron crystals. In addition, there exist two semicircles for pH_2 form 20% to 60%, the low frequency semicircle shows a trend of increase with lower pH_2, it may be related with H_2 diffusion resistance. The coupling of nano metal with surface oxygen vacancy is expected to create heterogeneous electrocatalytic sites and therefore improve the electrode performances. Similar behaviour has also been observed for both STNMO and STNMFO composite electrode in the symmetric cells in CO/CO_2 atmosphere with different CO partial pressure (pCO) ranging from 1% to 5% as shown in Fig. 11. In this case, a stronger reducing atmosphere of higher content CO is also favourable to increasing electrical conductivity of the reduced STNMO and STNMFO leading to improved electrode performances. The R_p of the symmetrical cell based on STNMO decreases from approximately 42.38 to 11.3 Ω·cm^2 as the pCO ranges from 1% to 5% while the R_p based on STNMFO improves from 17.42 to 2.59 Ω·cm^2 under the same conditions. Likewise, there are two semicircles in Fig. 11 (b1), it also may be related with CO diffusion resistance. This redox-stable electrode still shows the promising polarizations even in a less reducing atmosphere, which is necessary for high temperature direct electrolysis of carbon dioxide.

The direct electrolysis of pure carbon dioxide is studied in solid oxide electrolyzers with cathodes based on STNMFO and STNMO under a series of applied voltages ranging from 1.0 to 2.0 V at 800 ^{o}C, respectively. In order to check the sealing of the single solid oxide electrolyzer, the open circuit voltage (OCV) is recorded with the cathode and anode exposed to 5%H_2/Ar and static air, respectively, to check the separation between the anodic and cathodic gases. The OCVs reach about 1.0 V for the cells, which indicates a good separation between

the anodic and cathodic gas. Fig. 12 (a) shows the typical curves of the current density *versus* voltage (I-V curves) of the electrolyzers for direct carbon dioxide electrolysis. The maximum current density reaches about 252.6 $mA \cdot cm^{-2}$ at 2.0 V based on the STNMO cathode at 800 °C while the current density with STNMFO cathode is greatly improved to approximately 330.2 $mA \cdot cm^{-2}$ under the same conditions. Above 1.0 V, the current densities of the STNMFO composite electrodes increase steeply comparing with the STNMO composite cathode, which indicates that the coupling of nano metal with surface oxygen vacancy significantly enhances the cell performance for CO_2 electrolysis. The exsolution of iron nanoparticles is beneficial to the improvement of the electrode performance while the surface oxygen vacancy is favorable for the chemical adsorption of carbon dioxide. The enhanced ionic conductivity of the STNMFO is also expected to improve the charge transfer in the electrode/YSZ interfaces. In order to study the electrolysis performance with STNMFO and STNMO cathodes, cells are conducted with the composite cathodes fed pure CO_2 at 800 °C as shown in Fig. 12 (b). The current density with STNMFO/SDC cathode reaches 96.8, 144.6, 196.1, 251.4 and 314.2 $mA \cdot cm^{-2}$ at 1.2 to 2.0 V, respectively, which are much higher in contrast to the cell with STNMO cathode under the same conditions. Hence, the STNMFO composite cathode shows higher performances than STNMO at the electrolysis voltages which can enhance the direct carbon dioxide electrolysis.

For further study of the anticipated change in R_s and R_p, as shown in Fig. 13, the *in-situ* AC impedance spectroscopy is conducted under a series of applied voltages ranging from 1.0 to 2.0 V at 800 °C based on STNMFO and STNMO cathodes, respectively. It is observed that R_s values are general stable, whereas R_p values obviously decrease as applied voltages increase from 1.0 to 2.0 V. It is assumed that increasing the voltage improves the electrode performances that R_p decreases remarkably. Increasing the voltage is expected to improve electrode polarization, following the improved kinetic process of the electrode. The applied voltage electrochemically reduces the composite cathode to enhance the mixed conductivity and therefore accordingly enhances the electrocatalytic activity of the composite electrode. At high frequency, R_1 of the solid oxide electrolyzers with cathodes based on bare STNMO is decreased to approximately 0.46 $\Omega \cdot cm^2$. In contrast, the R_1 for the cell with STNMFO cathode is decreased to approximately 0.25 $\Omega \cdot cm^2$ and is further enhanced under high applied potentials. The improved R_1 firmly indicates that the increased oxide-ion conductivity of STNMFO significantly benefits the charge transfer. The R_2 for the cell based on STNMO cathode remarkably improves from 2.95 to 0.81 $\Omega \cdot cm^2$ with the applied voltage ranges from 1.0 to 2.0 V, suggesting the improved kinetics of gas conversion at high voltages. In contrast, the R_2 is based on STNMFO cathode significantly reduced to 2.51 $\Omega \cdot cm^2$ at low voltages and further enhanced to 0.49 $\Omega \cdot cm^2$ at high voltages demonstrating the significantly improved mass transfer due to the remarkable chemical adsorption of CO_2 in the composite cathode. The results indicate that the coupling of nano metal with surface oxygen vacancy largely improves the electrical performances of the composite cathode in solid oxide carbon dioxide electrolyzer.

Fig. 14 shows the rate of CO production and the current efficiency of the electrolyzers with cathodes based on STNMFO and STNMO for CO_2 electrolysis at different applied voltages. As shown in Fig. 14 (a), the maximum CO production for the cell based on STNMFO electrode is 1.971 $ml \cdot min^{-1} \cdot cm^{-2}$, which is much higher than 1.358 $ml \cdot min^{-1} \cdot cm^{-2}$ at 2.0 V with STNMO electrode. As shown in Fig. 14 (b), for the STNMO

cathode, the maximum current efficiencies reach 79.96% in the flow of CO_2 at 800 ^oC. In contrast, the maximum current efficiencies of the cell based on STNMFO cathode are enhanced to 92.2% under the same conditions. The current efficiency is largely improved by about 15% with exsolution of iron nanoparticles comparing with bare ceramic at high voltage. Obviously, the solid oxide electrolyzer based on STNMFO cathode exhibits better performance in contrast to the STNMO cathode. In order to validate the short-term stability of the STNMFO composite cathode, direct carbon dioxide electrolysis is performed at a fixed voltage of 1.6 V at 800 ^oC for 24 h with pure CO_2 fed the cathode. As shown in Fig. 15 (a), it reveals a slight decrease in the current density within the first few hours; however, the current density is stable (approximately 0.17 $A \cdot cm^{-2}$) on a general note, which confirms the excellent short-term stability of the STNMFO composite cathode for direct carbon dioxide electrolysis. In addition, SEM and EDS mapping, as shown in Fig.15 (b), are used to analyse the cathode surface after the short-term operation for high temperature carbon dioxide electrolysis. No microstructure crack is observed, which further confirms the material was stability. In addition, the XRD results of STNMO/SDC and STNMFO/SDC are shown in Fig. 16 (a) and (b), respectively. It is found that no other phase is appeared except for STNMO (or STNMFO), SDC and YSZ after CO_2 electrolysis test at 800 ^oC. Hence, the STNMO and STNMFO is chemically stable against SDC and YSZ at high temperature.

Conclusions

In this work, the *in-situ* growth of iron nanoparticles has been achieved to anchor on the redox-reversible STNMO ceramic substrate to combine the surface oxygen vacancy and form the heterogeneous catalysis clusters. The exsolution/dissolution of the iron nanoparticles is confirmed to be completely reversible in redox cycles. The ionic conductivity of iron-anchored reduced STNMO is significantly improved. The composite cathode achieves the direct carbon dioxide electrolysis at high temperature while the combined merit of metallic iron produces heterogeneous catalysis clusters to improve the current efficiency. The current efficiencies are enhanced by approximately 15% because of the coupling of nano metal with surface oxygen vacancy at high voltages for an oxide-ion conducting solid oxide electrolyzer at 800 ^oC.

Acknowledgements

This work is supported by the Natural Science Foundation of China No. 21303037, China Postdoctoral Science Foundation No. 2013M53150 and the Fundamental Research Funds for the Central Universities No. 2012HGZY0001.

Notes and references

[a] Department of Energy Materials, School of Materials Science and Engineering, Hefei University of Technology, No.193 Tunxi Road, Hefei, Anhui 230009, China.

[b] Key Laboratory of Advanced Functional Materials and Devices, Hefei University of Technology, No.193 Tunxi Road, Hefei, Anhui 230009, China.

*Corresponding: xiekui@hfut.edu.cn; ycwu@hfut.edu.cn

† Footnotes should appear here. These might include comments relevant to but not central to the matter under discussion, limited experimental and spectral data, and crystallographic data.

Electronic Supplementary Information (ESI) available: [details of any supplementary information available should be included here]. See DOI: 10.1039/b000000x/

1 C. Jiang, J. Ma, A. D. Bonaccorso and J. T. S. Irvine, *Energy Environ. Sci.*, 2012, **5**, 6973–6980.

2 S. Wang, A. Inoishi, J. Hong, Y. Ju, H. Hagiwara, S. Ida and T. Ishihara, *J. Mater. Chem. A*, 2013, **1**, 12455-12461.

3 C. Gaudillere, L. Navarrete and J. M. Serra, *Int. J. Hydrogen Energy*, 2014, **39**, 3047-3054.

4 M. Chen, J. V. T. Hogh, J. U. Nielsen, J. J. Bentzen, S. D. Ebbesen and P. V. Hendriksen, *Fuel Cells*, 2013, **4**, 638-645.

5 K. R. Sridhar and B. T. Vaniman, *Solid State Ionics*, 1997, **93**, 321-328.

6 H. Zhang, J. Wang, S. Su and J. Chen, *Int. J. Hydrogen Energy*, 2013, **38**, 9609-9618.

7 P. Kim-Lohsoontorn and J. Bae, *J. Power Sources*, 2011, **196**, 7161-7168.

8 S. D. Ebbesen and M. Mogensen, *J. Power Sources*, 2009, **193**, 349-358.

9 Y. Gan, J. Zhang, Y. Li, S. Li, K. Xie and J. T. S. Irvine, *J. Electrochem. Soc.*, 2012, **159**, F763-F765.

10 R. Xing, Y. Wang, S. Liu and C. Jin, *J. Power Sources*, 2012, **208**, 276-281.

11 S. Xu, S. Li, W. Yao, D. Dong and K. Xie, *J. Power Sources*, 2013, **230**, 115-121.

12 Y. Li, Y. Gan, Y, Wang, K. Xie and Y. Wu, *Int. J. Hydrogen Energy*, 2013, 38, 10196-10207.

13 C. Savaniu and J. T. S. Irvine, J. Mater. Chem., 2009, **19**, 8119-8128.

14 Y. Li, J. Zhou, D. Dong, Y. Wang, J. Jiang, H. Xiang and K. Xie, *Phys. Chem. Chem. Phys.*, 2012, **14**, 15547-15553.

15 T. Kolodiazhnyi and A. Petric, *J. Electroceram.*, 2005, **15**, 5-11.

16 M. D. Gross, K. M. Carver, M. A. Deighan, A. Schenkel, B. M. Smith and A. Z. Yee, *J. Electrochem. Soc.*, 2009, **156**, B540-B545.

17 P. Blennow, A. Hagen, K. K. Hansen, L. R. Wallenberg and M. Mogensen, *Solid State Ionics*, 2008, **179**, 2047-2058.

18 P. Blennow, K. K. Hansen, L. R. Wallenberg and M. Mogensen, *Solid State Ionics*, 2009, **180**, 63-70.

19 X. Yue and J. T. S. Irvine, *J. Electrochem. Soc.*, 2012, **159**, F442-F448.

20 X. Yue and J.T.S. Irvine, *Solid State Ionics*, 2012, **225**, 131-135.

21 C. Graves, S. D. Ebbesen, M. Mogensen, *Solid State Ionics*, 2011, **192**, 398-403.

22 W. Qi, Y. Gan, D. Yin, Z. Li, G. Wu, K. Xie and Y. Wu, *J. Mater. Chem. A*, **DOI:** 10.1039/C4TA00344F.

23 H. S. Hong and S. Lee, *J. Alloy. Compd.*, 2012, **538**, 201-204.

24 S. Li, Q. Qin, K. Xie, Y. Wang and Y. Wu, *J. Mater. Chem. A*, 2013, **1**, 8984-8993.

25 Q. Qin, G. Wu, S. Chen, W. Doherty, K. Xie and Y. Wu, *Electrochim. Acta*, 2014, **127**, 215-227.

26 H. Xie, L. Wang, D. Luo and Y. Yang, *J. Mater. Sci.*, 2014, **49**, 3314-3321.

27 D. Neagu, G. Tsekouras, D. N. Miller, H. Menard and J. T. S. Irvine, *Nat. Chem.*, 2013, **5**, 916-923.

28 C. Zuo, S. E. Dorris, U. Balachandran and M. Liu, *Chem. Mater.*, 2006, **18**, 4647-4650.

29 A. Charline, D. Thibaud, J. Olivier and G. Gilles, *J. Power Sources*, 2013, **223**, 341-348.

30 G. Tsekouras, D. Neagu and J. T. S. Irvine, *Energy Environ. Sci.*, 2013, **6**, 256-266.

31 W. Qi, C. Ruan, G. Wu, Y. Zhang, Y. Wang, K. Xie and Y. Wu, *Int. J. Hydrogen Energy*, 2014, **39**, 5485-5496.

32 G. Xiao, S. Nuansaeng, L. Zhang, S. Suthirakun, A. Heyden, H. Loye and F. Chen, *J. Mater. Chem. A*, 2013, **1**, 10546-10552.

33 H. He, Y. Huang, J. Regal, M. Boaro, J. M. Vohs and R. J. Gorte, *J. Am. Ceram. Soc.*, 2004, **87**, 331-336.

34 G. Jung and T. Huang, *J. Mater. Sci.*, 2003, **38**, 2461-2468.

35 A. Endo, M. Ihara, H. Komiyama and K. Yamada, *Solid State Ionics*, 1996, **86-88**, 1191-1195.

36 X. Li, H. Zhao, F. Gao, Z. Zhu, N. Chen and W. Shen, *Solid State Ionics*, 2008, **179**, 1588-1592.

37 S. L. Wang, B. Lin, K. Xie, Y. C. Dong, X. Q. Liu, G. Y. Meng, *J. Alloy. Compd.*, 2009, **468**, 499-504.

38 K. Xie, R. Q. Yan, Y. Z. Jiang, X. Q. Liu, G. Y. Meng, *J. Membrane Sci.*, 2008, **325**, 6-10.

Captions

Fig. 1: XRD rietveld refinement patterns of samples, (a1) Oxidized STNMO; (a2) Reduced STNMO; (b1) Oxidized STNMFO; (b2) Reduced STNMFO.

Fig. 2: TEM of the samples (a1) oxidized STNMO, (a2) reduced STNMO, (b1)oxidized STNMFO, (b2)reduced STNMFO.

Fig. 3: XPS results of STNMO, (a1) Ti in oxidized; (a2) Ti in reduced;(b1) Nb in oxidized; (b2) Nb in reduced;(c1) Mn in oxidized; (c2) Mn in reduced.

Fig. 4: XPS results of STNMFO, (a1) Ti in oxidized; (a2) Ti in reduced;(b1) Nb in oxidized; (b2) Nb in reduced;(c1) Mn in oxidized; (c2) Mn in reduced; (d1) Fe in oxidized; (d2) Fe in reduced.

Fig. 5: TG of samples in 5% H_2/Ar from 1000 ^oC to room temperature (RT), (a) STNO; (b) STNMO.

Fig. 6: XRD and SEM results of STNMO samples during redox cycle: (a1 and a2) XRD patterns of firstly oxidized and secondly reduced STNMO and (b1 and b2) SEM of the firstly oxidized and secondly reduced STNMO.

Fig. 7: XRD, SEM and EDS results of STNMFO samples during redox cycle: (a) XRD patterns of the firstly and secondly reduced STNMFO and (b1 and b2) SEM/EDS of the firstly and secondly reduced STNMFO.

Fig. 8: The ion conductivity of samples *versus* temperature from 400 to 800 ^oC, (a) STNMO; (b) STNMFO in oxidized and reduced situations.

Fig. 9: Microstructure of the solid oxide symmetric and electrolyzer cells (a1) STNMO/SDC-YSZ-STNMO/SDC, (a2) STNMFO/SDC-YSZ-STNMFO/SDC; (b1) STNMO/SDC-YSZ-LSMO/SDC, (b2) STNMFO/SDC-YSZ-LSMO/SDC.

Fig. 10: The AC impendence of the symmetric cells for (a1, a2) STNMO and (b1, b2) STNMFO in different pH_2 at 800 ^oC.

Fig. 11: The AC impendence of the symmetric cells for (a1, a2) STNMO and (b1, b2) STNMFO in different pCO at 800 ^oC.

Fig. 12: (a) The I-V curves of two electrolyzers at 800 ^oC in CO_2; (b) the performances of electrolysis for electrolyzer at 800 ^oC in CO_2.

Fig. 13: The *in-situ* AC impendence of the electrolysis cells based on (a1, a2) STNMO and (b1, b2) STNMFO in different voltage with the flow of CO_2 at 800 ^oC.

Fig. 14: (a) The production of CO; (b) current efficiency for the electrolyzers with STNMO and STNMFO in the flow of CO_2 at 800 ^oC.

Fig. 15: (a) Short-term performance of the electrolyzer based STNMFO/SDC cathode with the flow of CO_2 at 800 ^oC under 1.6 V applied voltage for CO_2 electrolysis; (b) SEM and EDS of STNMFO/SDC cathode surface after test.

Fig. 16: XRD results of composite cathode after CO_2 electrolysis at 800 ^oC, (a) STNMO/SDC-YSZ; (b) STNMFO/SDC-YSZ.

Fig. 1

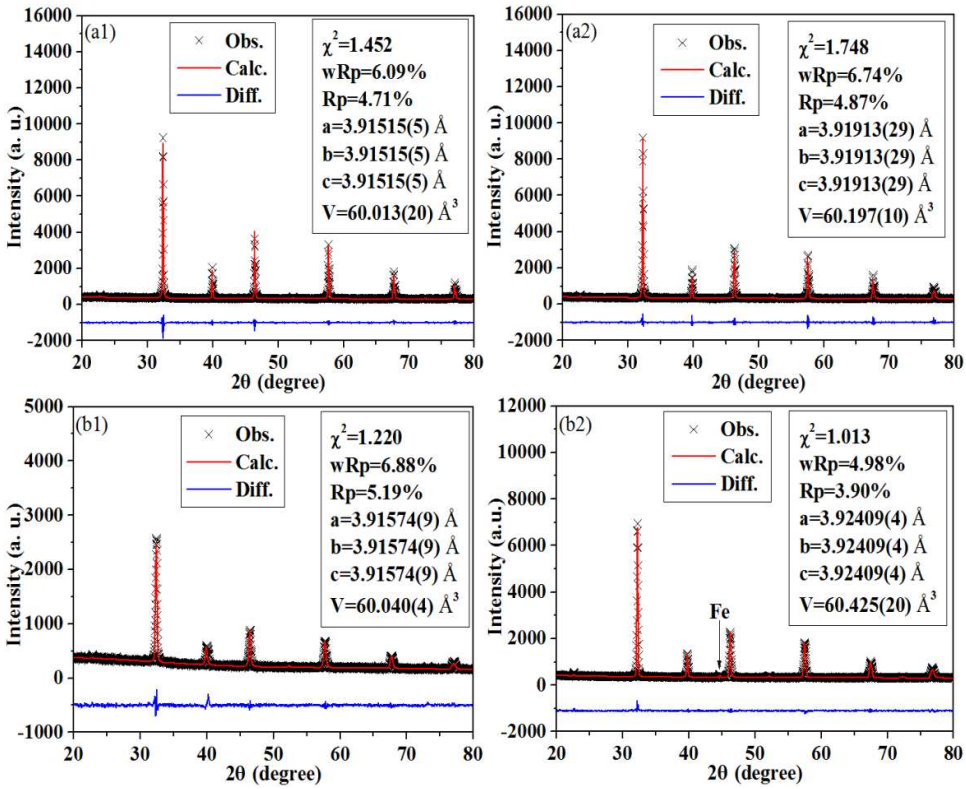

Fig. 2

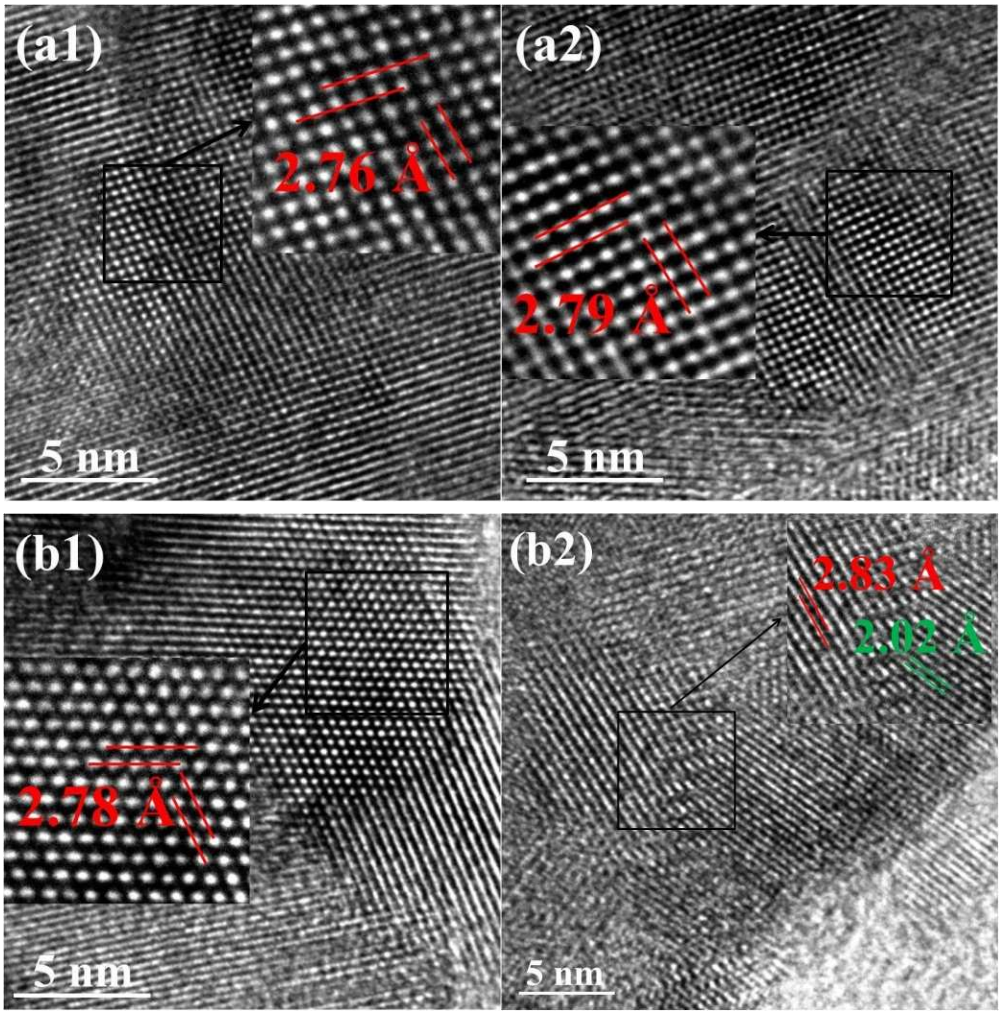

Fig. 3

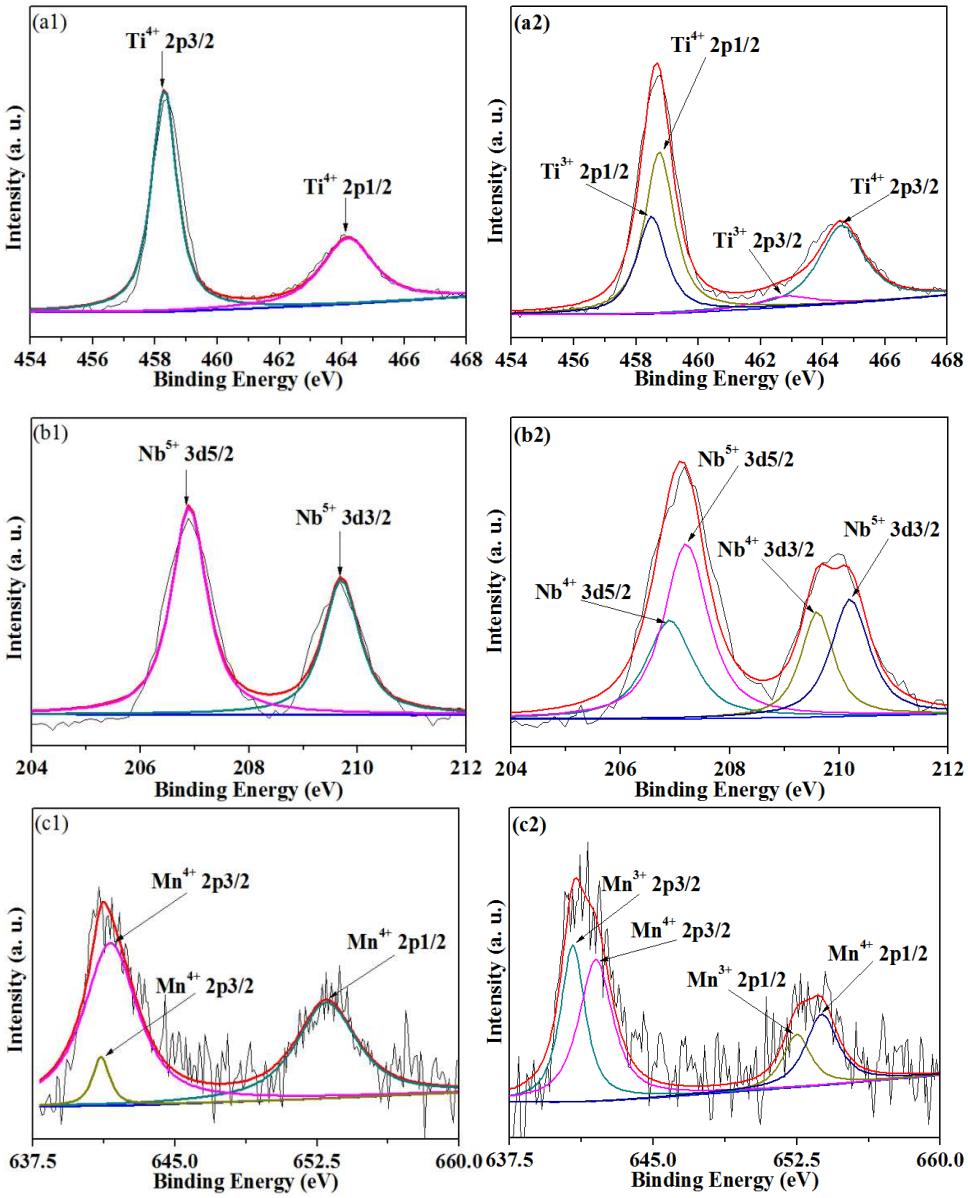

Fig. 4

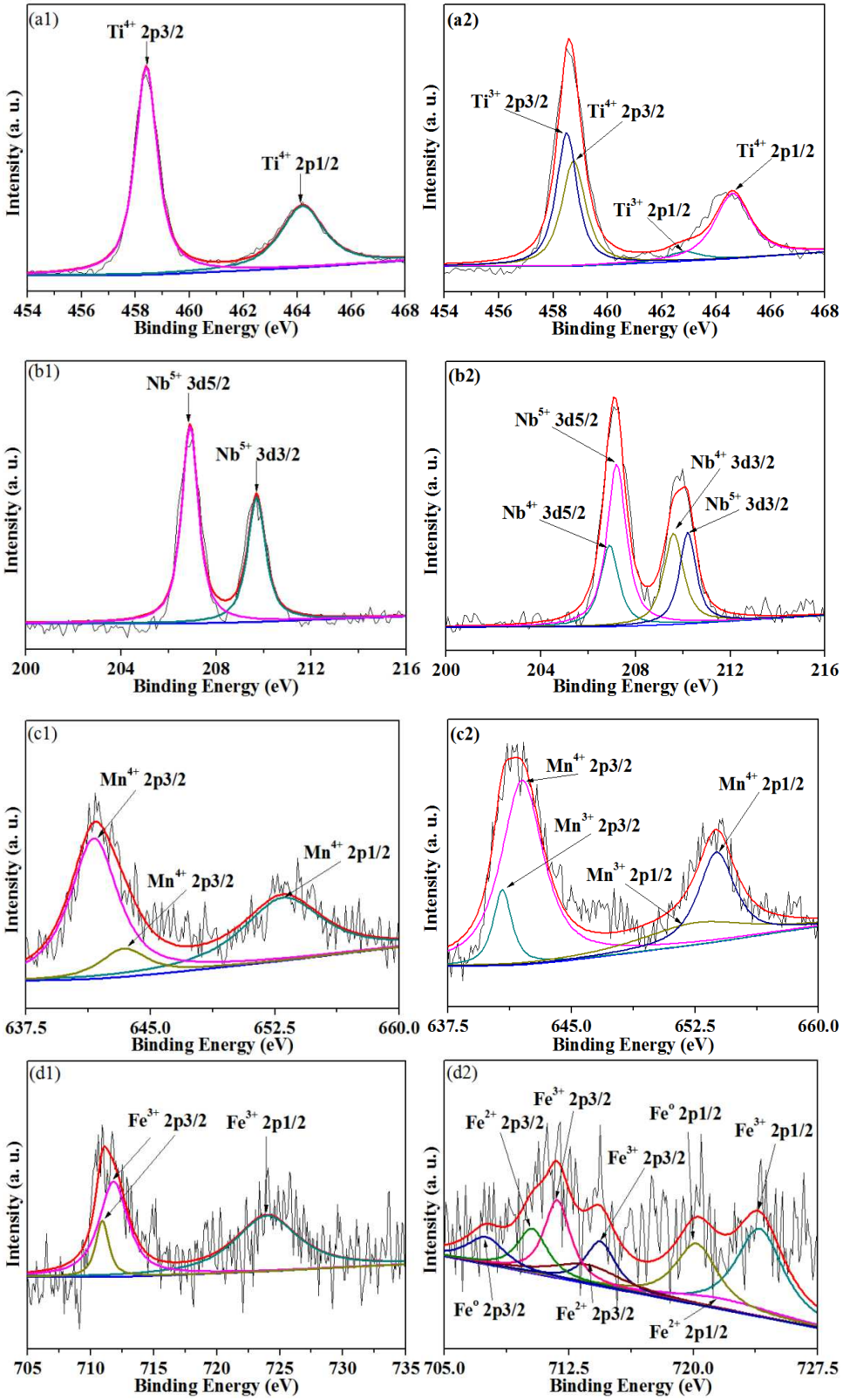

Fig. 5

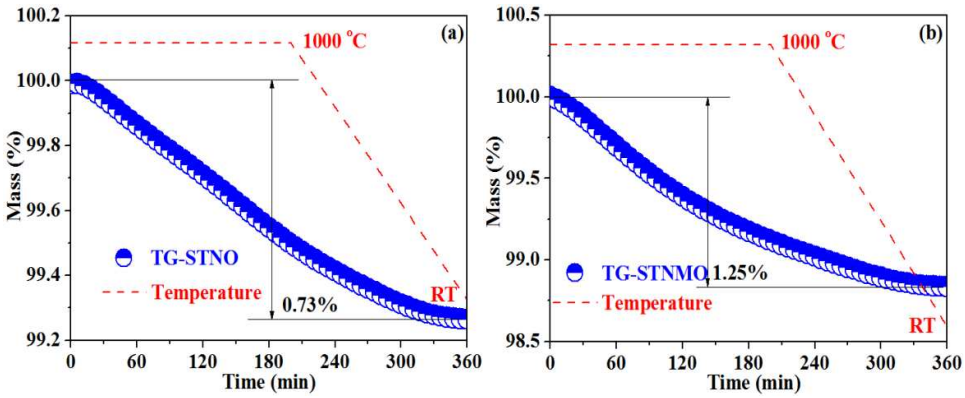

Fig. 6

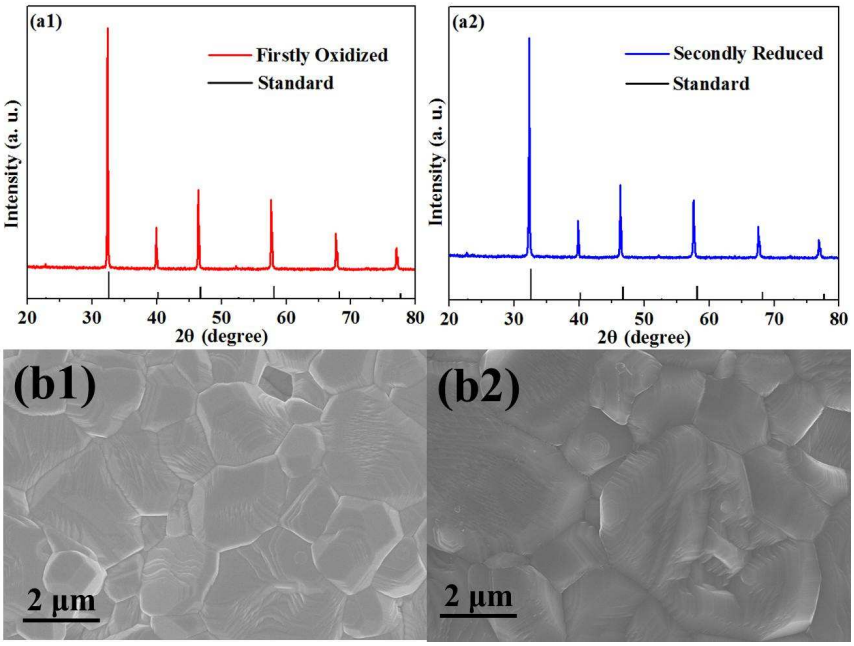

Fig. 7

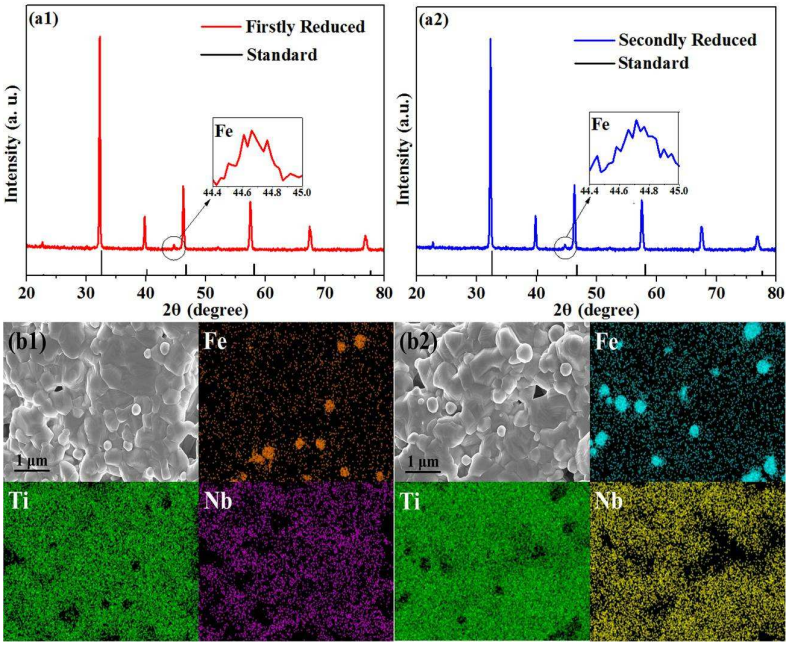

Fig. 8

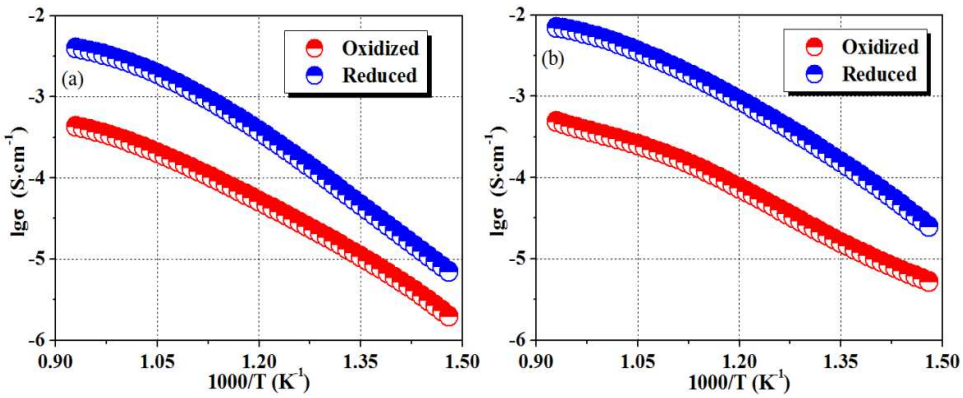

Fig. 9

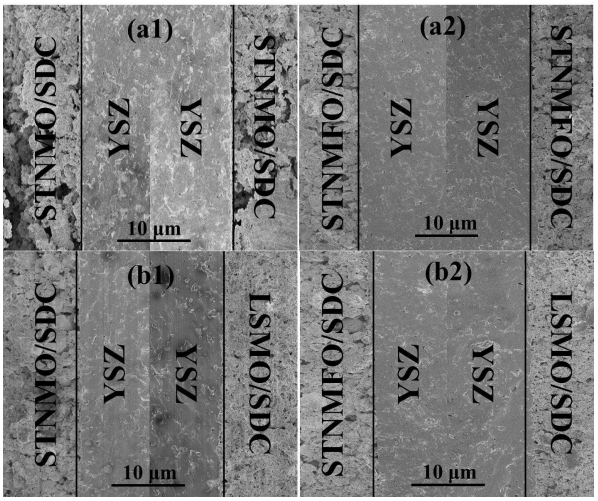

Fig. 10

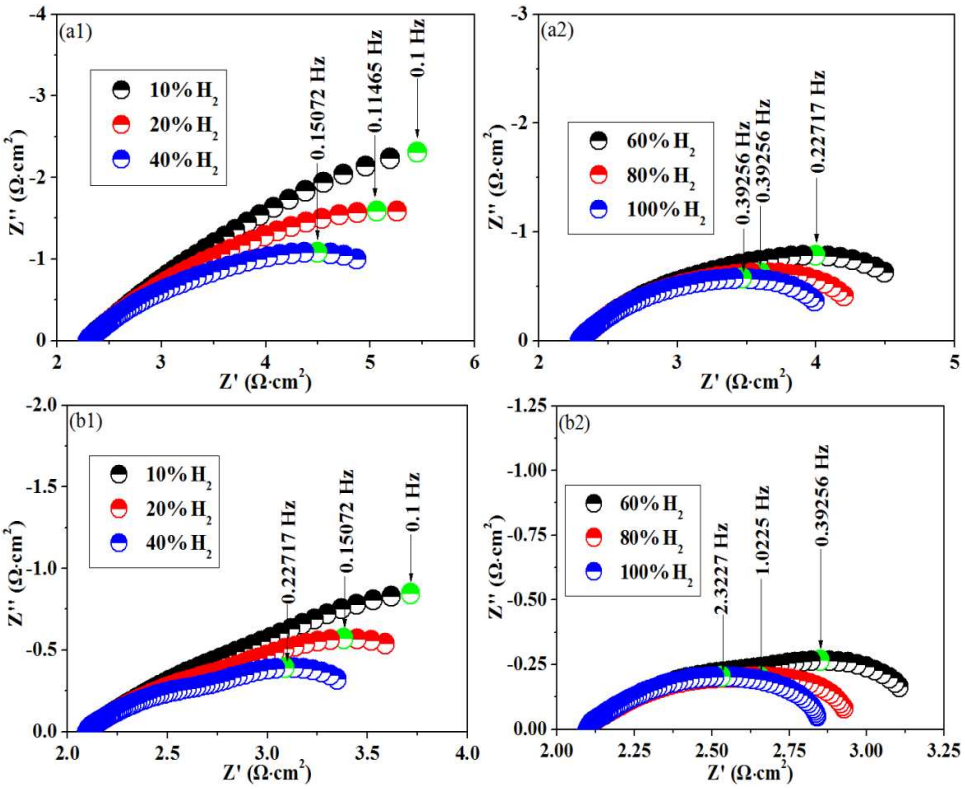

Fig. 11

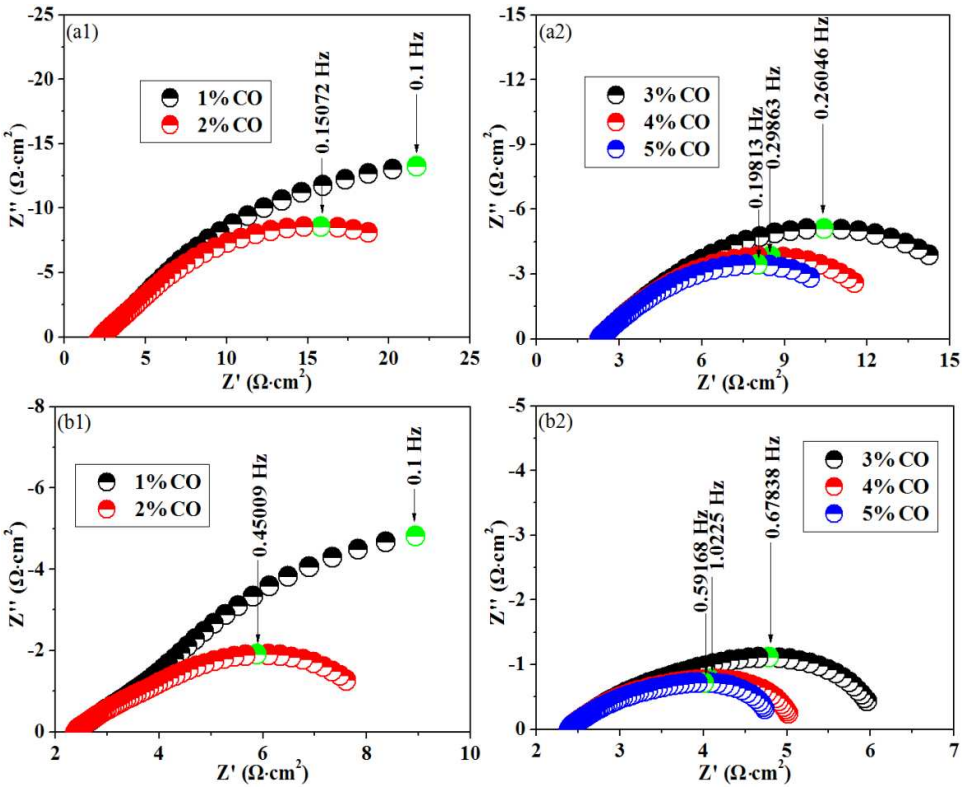

Fig. 12

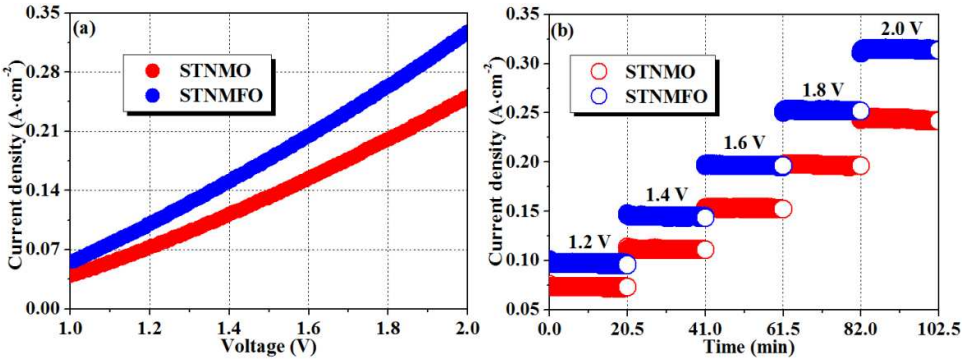

Fig. 13

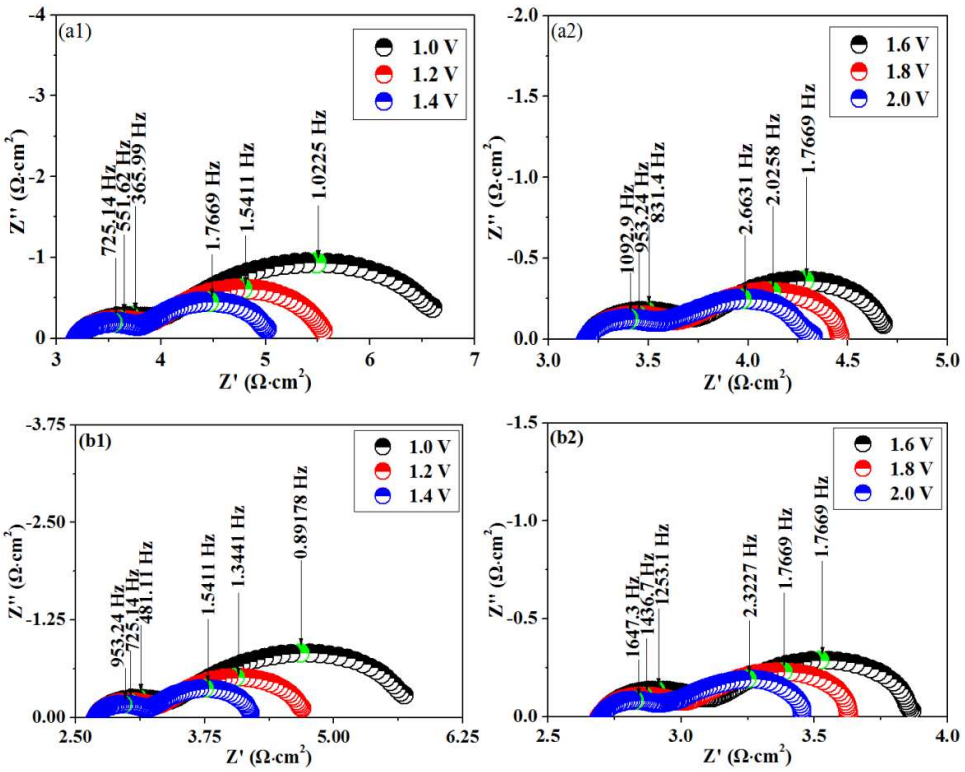

Fig. 14

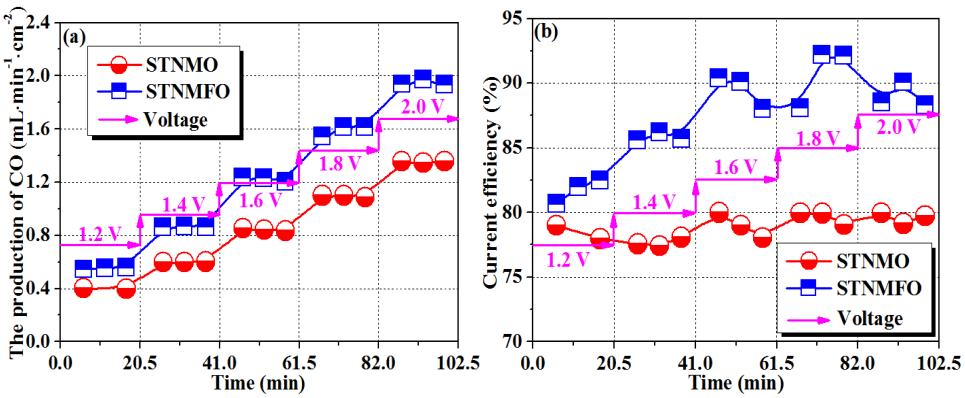

Fig. 15

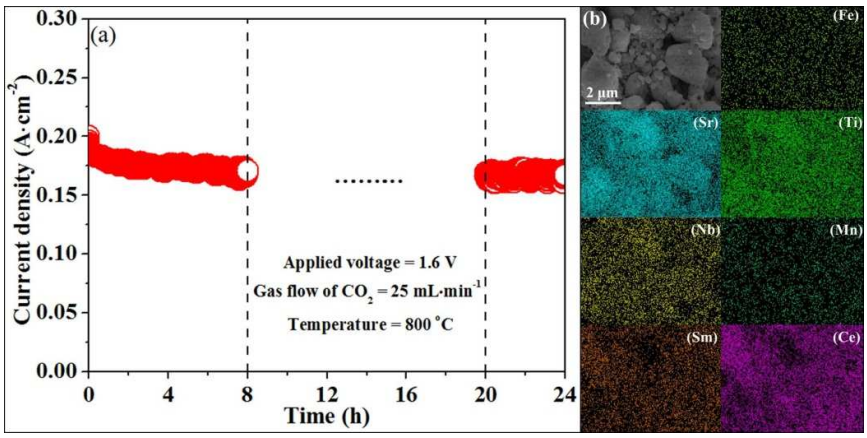

Fig. 16

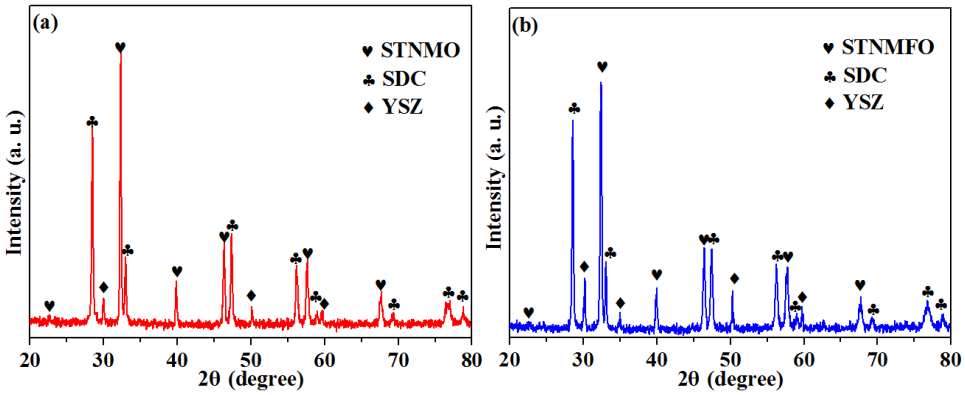

Table of Contents

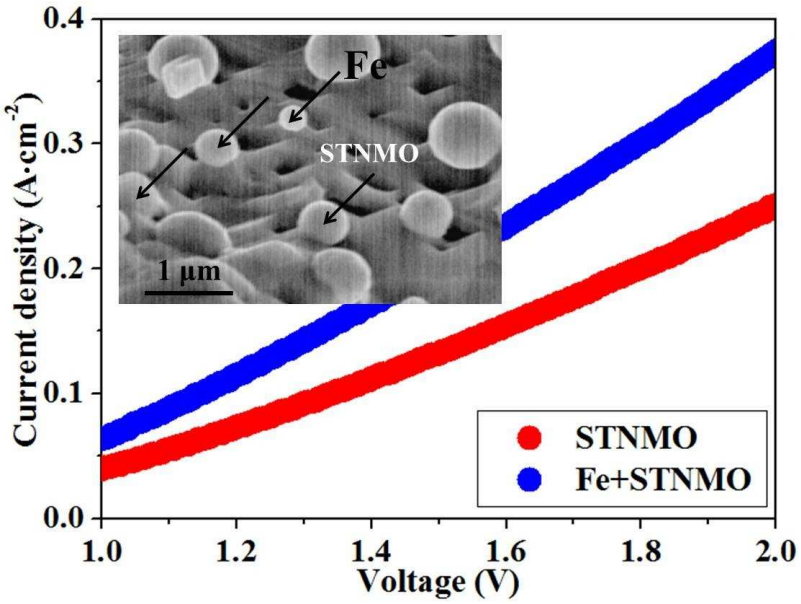

Significant improvement has been achieved with heterogeneous electrocatalytic sites towards efficient CO_2 electrolysis.